IEEE Access
Multidisciplinary ⋮ Rapid Review ⋮ Open Access Journal

Received 10 November 2023, accepted 5 December 2023, date of publication 7 December 2023,
date of current version 14 December 2023.

Digital Object Identifier 10.1109/ACCESS.2023.3340689

RESEARCH ARTICLE

220/293 GHz Dual-Band Anomalous Reflectors Using Higher-Order Diffraction Modes and Their Precise Characterization Using a Compact Antenna Test Range System

YUTO KATO[1], (Member, IEEE), MICHITAKA AMEYA[1], (Member, IEEE), MASAO TEZUKA[2], HISASHI KOBUKE[2], AND ATSUSHI SANADA[3], (Member, IEEE)

[1]Research Institute for Physical Measurement, National Institute of Advanced Industrial Science and Technology, Ibaraki 305-8563, Japan
[2]Electronic Components BC, TDK Corporation, Tokyo 103-6128, Japan
[3]Graduate School of Engineering Science, Osaka University, Osaka 560-8531, Japan

Corresponding author: Yuto Kato (y-katou@aist.go.jp)

This paper is based on results obtained from "Research and Development Project of the Enhanced Infrastructures for Post-5G Information and Communication Systems" (JPNP20017), commissioned by the New Energy and Industrial Technology Development Organization (NEDO).

ABSTRACT We propose dual-band anomalous reflectors operating at 220 GHz and 293.3 GHz for 6G applications. The anomalous reflectors consist of paired patch elements on single-layer and via-free substrates. Based on a local reflection phase design and optimization of paired patch elements, higher-order diffraction modes can be controlled simultaneously at the two harmonic frequencies to achieve highly efficient dual-band anomalous reflections in identical directions with wide reflection angles. Two reflectors are designed and fabricated on cyclo-olefin polymer (COP) substrates for the reflection angles of 45° and 50° and the incident angles of 0° and −10°, respectively. To evaluate their anomalous reflection performances under plane wave illumination in the J-band, we develop a compact reflector characterization system in the J-band exploiting a compact antenna test range (CATR) technique consisting of an offset Gregorian antenna. The developed CATR-based system generates a quasi-plane wave with a beam diameter of approximately 250 mm at 300 GHz at a position 900 mm from the antenna, enabling precise far-field bistatic radar cross section (BRCS) measurements with a compact system size. The measured BRCSs of the prototypes are in good agreement with the simulated results and highly efficient dual-band anomalous reflection operations are experimentally demonstrated with the efficiencies of over 80 % excluding the material losses in both the designed bands.

INDEX TERMS Anomalous reflectors, compact antenna test range, dual-band operation, J-band, metasurfaces, millimeter-wave, terahertz, 6G communication.

I. INTRODUCTION

In the sixth generation (6G) wireless communication using the sub-terahertz and terahertz bands, metasurface-based anomalous reflectors that reflect incident waves toward specified directions that do not adhere to the law of reflection are attracting attentions to achieve quasi-line-of-sight communications by bypassing physical obstacles with flexible deployments [1], [2], [3], [4], [5], [6], [7], [8], [9], [10]. Multiband capabilities are needed for anomalous reflectors considering the demand for the carrier aggregation in wireless communications.

Dual-band anomalous reflectors have been realized by using multi-layer substrates at 28 GHz/39 GHz to realize desired local reflection phase distributions for each target frequency band [11]. However, owing to difficulties in

The associate editor coordinating the review of this manuscript and approving it for publication was Bilal Khawaja.

alignment between layers, single-layer implementation is desirable for 6G applications above 100 GHz. Single-layer dual-band anomalous reflectors have been proposed at 10 GHz/15 GHz by introducing interleaved metagrating with via fences to suppress mutual coupling [12]. However, owing to the fabrication complexity and extra losses of vias, it is also difficult to apply the structure for 6G applications. Conventional reflectarrays [13], [14], [15], [16], [17], [18] might be applied for dual-band anomalous reflectors for 6G applications with single-layer and via-free structures. However, the element sizes of the reflectarrays for controlling the local reflection phase are generally comparable to or longer than 0.5 wavelength; thus, they have a fundamental limitation in the maximum reflection angle and efficiency, which is not favorable for coverage expansion applications in 6G communication. For instance, the reflection angles of the reflectarray in [18] at 28.7 GHz and 32.8 GHz are only 15° and 30°, respectively.

Precise reflector characterization is also important for the development of anomalous reflectors especially in the sub-terahertz and terahertz bands. Considering that a reflector is illuminated from a distant base station antenna in a practical use environment and that reflector performances are optimized for plane wave illumination in the designs, it is desirable for anomalous reflectors to be characterized under plane wave illumination. Conventional free-space measurement setups often suffer from effects of amplitude and phase non-uniformities of an incident beam due to an insufficient distance between a transmitting antenna and a reflector under test to achieve flat amplitude and phase distributions [8], [10]. A large measurement system for plane wave illumination involves large propagation losses and is impractical. A compact antenna test range (CATR) system is a promising solution for the reflector characterization under plane wave illumination. A CATR system, which consists of a feed antenna-coupled collimating optic that can generate a quasi-plane wave at a close range, has been widely used for far-field antenna characterization [19], [20], [21], [22]. Although there have been reports on reflector characterization with a CATR-based system in the microwave and lower millimeter-wave regions [11], [23], there are no reports above 100 GHz for 6G applications.

In this paper, we propose dual-band anomalous reflectors operating at 220 GHz and 293.3 GHz for 6G applications. The proposed reflectors consist of paired patch elements on single-layer and via-free substrates. Based on a local reflection phase design and optimization of paired patch elements, higher-order diffraction modes can be controlled simultaneously at the two harmonic frequencies to achieve highly efficient dual-band anomalous reflections in identical directions with wide reflection angles. Two reflectors are designed on cyclo-olefin polymer (COP) substrates for the reflection angles of 45° and 50° and the incident angles of 0° and −10°, respectively. Here, the target frequencies of 220 GHz and 293.3 GHz are selected because they are within the promising frequency bands for 6G communications [24], [25] with the ratio of 3:4. To evaluate the anomalous reflection performances of the designed dual-band reflectors under plane wave illumination in the J-band, we develop a compact reflector characterization system exploiting the CATR technique consisting of an offset Gregorian antenna. After evaluating the system performance, the dual-band anomalous reflection performances of the fabricated reflectors are characterized with the CATR-based system in the J-band.

The remainder of this paper is organized as follows. In Section II-A, we present the configuration of the dual-band anomalous reflector and design two reflectors for the reflection angles of 45° and 50° and the incident angles of 0° and −10°, respectively. Dual-band anomalous reflection performances of the designed reflectors are numerically investigated in Section II-B. In Section III, we present the configuration and performance of the developed CATR-based reflector characterization system. The designed dual-band reflectors are fabricated, and the reflection characteristics are measured to evaluate anomalous reflection efficiencies in Section IV. Finally, conclusions are presented in Section V.

II. DUAL-BAND ANOMALOUS REFLECTORS USING HIGHER ORDER MODES

A. DUAL-BAND UNIT CELL DESIGN

The dual-band anomalous reflector is designed so that it reflects a y-polarized incident wave with the incident angle θ_I into the target reflection angle θ_R at the two operating frequencies of 220 GHz and 293.3 GHz with suppressed parasitic reflections as shown in Fig. 1(a). The reflector consists of a 2-D array of unit cells shown in Fig. 1(b) with linearly arranged 12 metallic paired patch elements on a dielectric substrate backed by a metallic ground plane as shown in Fig. 1(c). The third and fourth diffraction modes are selectively excited in the unit cell at 220 GHz and 293.3 GHz, respectively, to induce anomalous reflections in the same direction at the two operating frequencies with the ratio of 3:4. By controlling the local reflection phase with the paired patch dimensions, 6π and 8π phase shifts are introduced along the x-direction in the unit cell at 220 GHz and 293.3 GHz, respectively, to realize the selective excitation of the diffraction modes. The periods of the unit cell in the x- and y-directions are determined by $D_x = 4\lambda_0/|\sin\theta_\mathrm{I} - \sin\theta_\mathrm{R}|$ and $D_y = \lambda_0/2$, respectively, where $\lambda_0 = 1.02$ mm is the free space wavelength at 293.3 GHz. A copper-clad cyclo-olefin polymer (COP) substrate is used as the substrate material. The thicknesses of the substrate and metallic layers are $t = 0.05$ mm and $t_\mathrm{c} = 12\,\mu$m, respectively. The material parameters used in the design are: the relative permittivity of 2.33, loss tangent of 3.7×10^{-4}, and conductivity of 2.0×10^7 S/m [8].

We design a dual-band anomalous reflector for $(\theta_\mathrm{I}, \theta_\mathrm{R}) = (0°, 45°)$. To independently control the reflection phases of the element at 220 GHz and 293.3 GHz, we calculate the

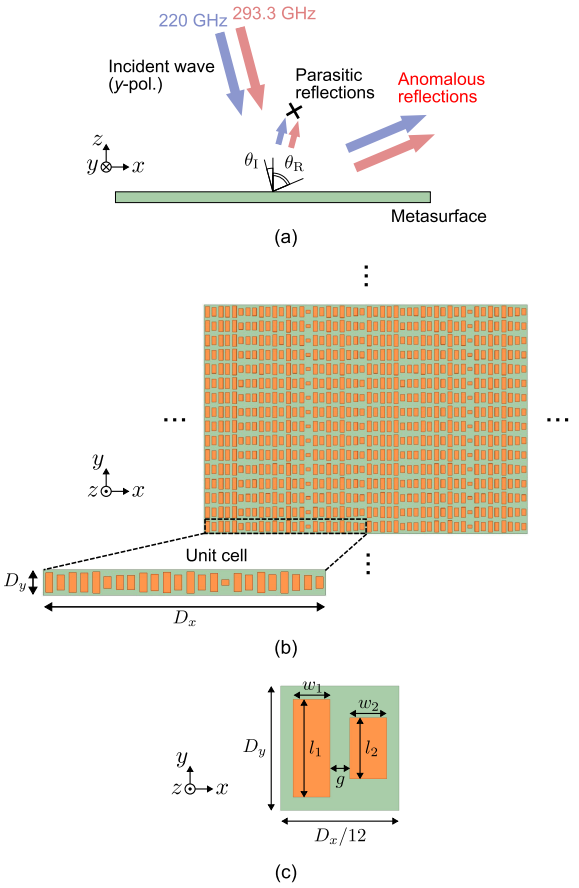

FIGURE 1. Proposed dual-band anomalous reflector. (a) Dual-band operation of an anomalous reflector. (b) Top view of the reflector consisting of a 2-D array of unit cells. (c) Paired patch element.

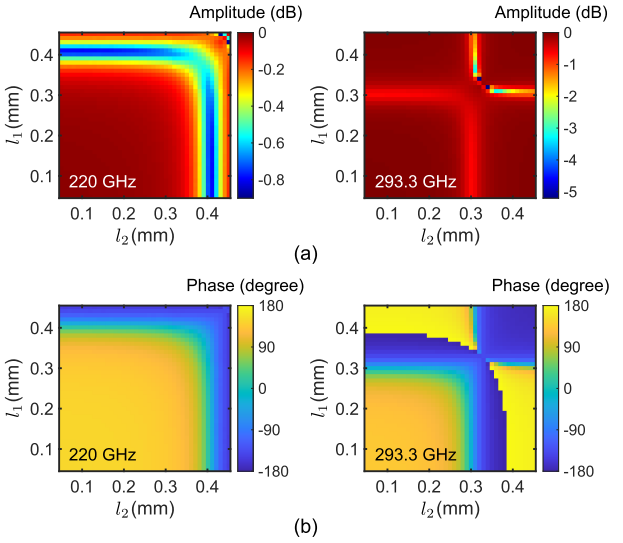

FIGURE 2. Simulated relationships between the patch lengths (l_1, l_2) and the reflection characteristics of the paired patch element for normal incident waves ($\theta_I = 0°$) at 220 GHz and 293.3 GHz. (a) Amplitude. (b) Phase.

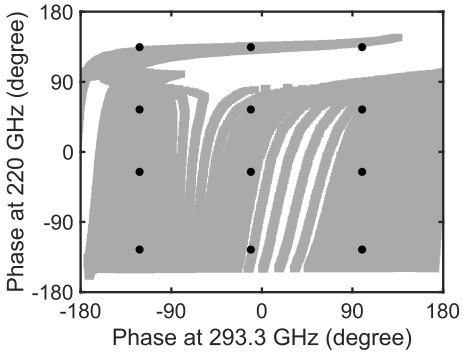

FIGURE 3. Phase range that can be implemented by the paired patch element with a phase tolerance of ±5° at the two frequencies (represented by a gray area). Black markers: target phases for the initial design.

reflection characteristics of the element at the two frequencies for various l_1 and l_2 values ranging from 0.05 mm to 0.45 mm, where other dimensions are fixed at $w_1 = w_2 = 0.15$ mm and $g = 0.08$ mm (see Fig. 1(c)). Fig. 2 shows the relationships between the patch lengths and the reflection characteristics for normal incident waves ($\theta_I = 0°$) at 220 GHz and 293.3 GHz obtained by full-wave simulations using the HFSS under 2-D periodic boundary conditions. The phases at the two frequencies can be controlled almost independently by utilizing the degree of design freedom with the paired patch element. Based on the analysis of Fig. 2(b), we obtain the gray area in Fig. 3 representing reflection phases at the two frequencies realized by the paired patch element with a phase tolerance of ±5°. It is seen from Fig. 3 that approximately 66 % of the entire phase plane is realized by the element structure with the maximum loss of −5.2 dB (see Fig. 2(a)).

The local reflection phases at the two frequencies for the desired dual-band anomalous reflection are theoretically given from D_x, θ_I, and θ_R [1]. By using the degree of freedom of phase offsets that can be adjusted independently for the two frequencies, the target phases for the 12 elements are determined to be at the black markers within the gray area as shown in Fig. 3. The corresponding patch lengths are determined from Fig. 2(b). The unit cell structure thus derived is shown in Fig. 4(a).

With the designed patch lengths as *'initial guess'*, all 24 patch lengths are optimized by calculating the reflection coefficients of the diffraction modes for the unit cell by full-wave simulations under 2-D periodic boundary conditions. Since the reflection from the normal incident waves ($\theta_I = 0°$) to the desired θ_R direction corresponds to the reflections from the zeroth to third and fourth diffraction modes at 220 GHz and 293.3 GHz, respectively, we set the optimization goal as $\left|S_{11}^{0\to3}\right|^2$ (at 220 GHz) $= \left|S_{11}^{0\to4}\right|^2$ (at 293.3 GHz) $= 1$, where $S_{11}^{0\to m}$ is the reflection coefficient between the zeroth and m-th diffraction modes. Toward this goal, optimization of the lengths of 24 patches is proceeded based on the quasi-Newton method using iterative full-wave simulations. The number of propagating diffraction modes considered in the

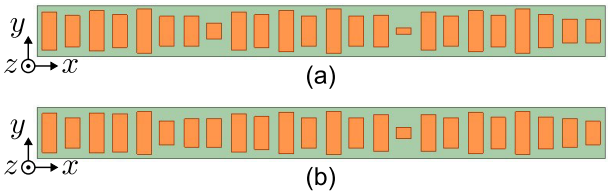

FIGURE 4. (a) Initial and (b) optimized unit cells of the dual-band anomalous reflector with $(\theta_I, \theta_R) = (0°, 45°)$.

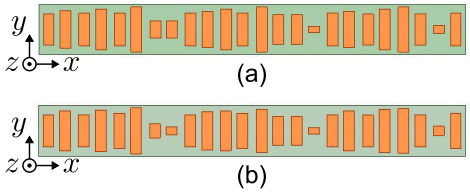

FIGURE 5. (a) Initial and (b) optimized unit cells of the dual-band anomalous reflector with $(\theta_I, \theta_R) = (-10°, 50°)$.

simulations is 11 with m ranging from -5 to 5. The optimized unit cell structure is shown in Fig. 4(b).

As another design example, we design a dual-band anomalous reflector at 220 GHz and 293.3 GHz for $(\theta_I, \theta_R) = (-10°, 50°)$ by following the same procedure. Note that the steering reflection angle defined by $|\theta_I - \theta_R|$ of the second design is larger than that of the first design. With a decreased D_x, the number of propagating diffraction modes to be considered in the simulations decreases to 8 with m ranging from -3 to 4. The initial and optimized unit cells for this design are shown in Fig. 5(a) and (b), respectively.

B. SIMULATED DUAL-BAND REFLECTOR PERFORMANCES

To investigate reflected powers of the anomalous and parasitic reflections, $\left|S_{11}^{0\to m}\right|^2$ are calculated at 220 GHz and 293.3 GHz for the initial and optimized designs. Fig. 6(a) shows the results for the reflectors with $(\theta_I, \theta_R) = (0°, 45°)$. Note that the reflected powers of the desired anomalous reflections correspond to $\left|S_{11}^{0\to 3}\right|^2$ and $\left|S_{11}^{0\to 4}\right|^2$ at 220 GHz and 293.3 GHz, respectively. As seen from Fig. 6(a), for the initial design, a major part of the total reflected power is directed to the desired anomalous reflection for each frequency with some parasitic reflections of other diffraction modes. In contrast, the unit cell optimization successfully improves the anomalous reflection efficiencies with significantly suppressed parasitic reflections in undesired directions.

Fig. 6(b) shows the results for the reflectors with $(\theta_I, \theta_R) = (-10°, 50°)$. For the initial design, the desired third diffraction mode has the largest reflected power at 220 GHz, while the fourth mode is the second largest at 293.3 GHz after zeroth specular reflection. Even in this case, the optimized design achieves significant suppression of the parasitic reflections with most of the reflected power selectively directed to the desired third/fourth diffraction modes corresponding to the anomalous reflections.

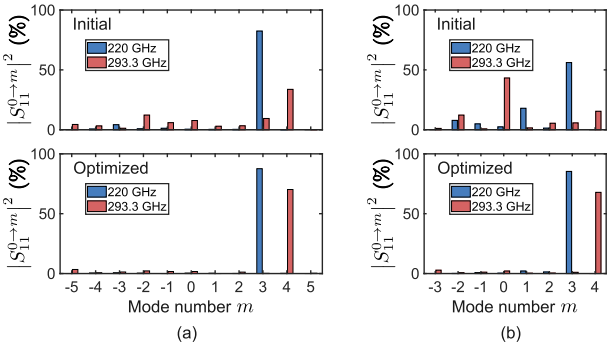

FIGURE 6. Simulated $\left|S_{11}^{0\to m}\right|^2$ at 220 GHz and 293.3 GHz for the initial and optimized designs of the anomalous reflectors with (a) $(\theta_I, \theta_R) = (0°, 45°)$ and (b) $(\theta_I, \theta_R) = (-10°, 50°)$.

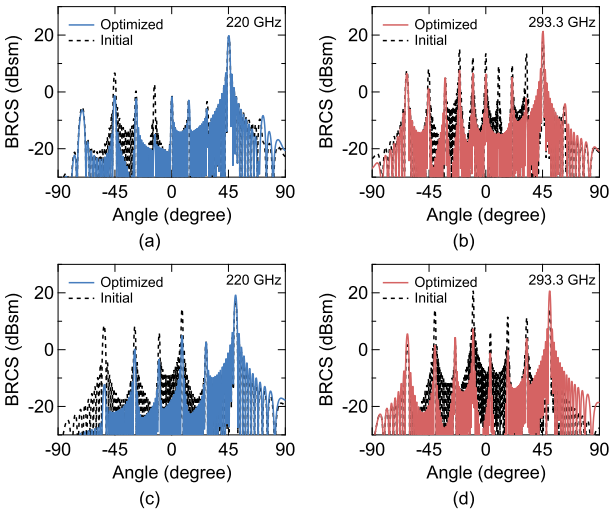

FIGURE 7. Simulated BRCSs for the designed reflectors. Results for the optimized and initial designs with $(\theta_I, \theta_R) = (0°, 45°)$ consisting of 12 × 136 unit cells at (a) 220 GHz and (b) 293.3 GHz. Results for the optimized and initial designs with $(\theta_I, \theta_R) = (-10°, 50°)$ consisting of 16 × 136 unit cells at (c) 220 GHz and (d) 293.3 GHz.

The total loss of a reflector is caused by two mechanisms: the energy leakage to the parasitic reflections and the material losses in the substrate (dielectric and conductor losses). The former and latter contributions are numerically evaluated by calculating $\sum_{m\neq m^*}\left|S_{11}^{0\to m}\right|^2$ ($m^* = 3, 4$ at 220 GHz and 293.3 GHz, respectively) and $\left(1-\sum_m\left|S_{11}^{0\to m}\right|^2\right)$, respectively. Table 1 shows the simulated efficiencies with the two loss contributions and the efficiencies excluding the material losses $\left(=\left|S_{11}^{0\to m^*}\right|^2/\sum_m\left|S_{11}^{0\to m}\right|^2\right)$ for the designed reflectors with $(\theta_I, \theta_R) = (0°, 45°)$. As seen from the table, the unit cell optimization significantly suppresses the parasitic reflections at the expense of a slight increase in the material losses. This leads to anomalous reflection efficiency improvements. The efficiencies for the optimized design are 87.6 % and 70.6 % at 220 GHz and 293.3 GHz, respectively. The efficiencies excluding the material losses are 97.2 % and 84.7 % at 220 GHz and 293.3 GHz,

TABLE 1. Simulation results of the efficiencies, loss contributions owing to parasitic reflections and material losses, and efficiencies excluding the material losses for the designed reflectors with $(\theta_I, \theta_R) = (0°, 45°)$.

	Frequency	Efficiency	Total parasitic reflection	Material loss	Efficiency excl. material loss
Initial design	220 GHz	82.4 %	7.9 %	9.7 %	91.3 %
	293.3 GHz	33.7 %	50.4 %	16.0 %	40.1 %
Optimized design	220 GHz	87.6 %	2.5 %	9.9 %	97.2 %
	293.3 GHz	70.2 %	12.7 %	17.1 %	84.7 %

TABLE 2. Simulation results of the efficiencies, loss contributions owing to parasitic reflections and material losses, and efficiencies excluding the material losses for the designed reflectors with $(\theta_I, \theta_R) = (-10°, 50°)$.

	Frequency	Efficiency	Total parasitic reflection	Material loss	Efficiency excl. material loss
Initial design	220 GHz	56.1 %	34.3 %	9.6 %	62.1 %
	293.3 GHz	15.4 %	70.0 %	14.6 %	18.1 %
Optimized design	220 GHz	85.3 %	4.5 %	10.2 %	95.0 %
	293.3 GHz	67.8 %	8.3 %	23.9 %	89.1 %

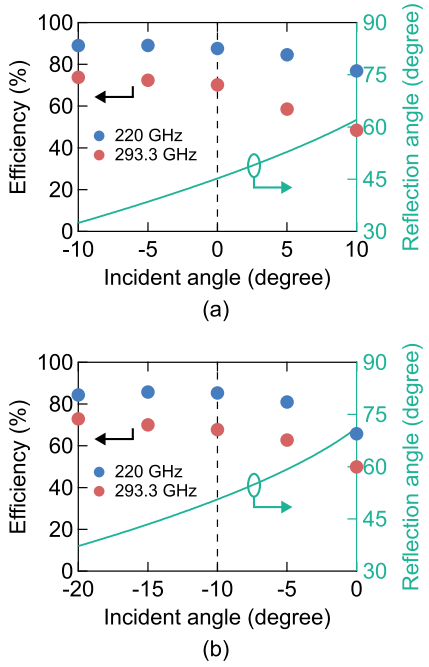

FIGURE 8. Simulated anomalous reflection efficiencies at 220 GHz and 293.3 GHz when the incident angle deviates from the designed value. Green lines: theoretical relationships between θ_i and θ_r. (a) Optimized design with $(\theta_I, \theta_R) = (0°, 45°)$. (b) Optimized design with $(\theta_I, \theta_R) = (-10°, 50°)$.

respectively. Table 2 shows the results for the designed reflectors with $(\theta_I, \theta_R) = (-10°, 50°)$. The tendencies of the two loss contributions before and after the optimization are similar to those of the designs with $(\theta_I, \theta_R) = (0°, 45°)$. The efficiencies for the optimized design are 85.3 % and 67.8 % at 220 GHz and 293.3 GHz, respectively. The efficiencies excluding the material losses are 95.0 % and 89.1 % at 220 GHz and 293.3 GHz, respectively. With these results, highly efficient dual-band operation of the designed anomalous reflectors is numerically demonstrated.

Moreover, the bistatic radar cross sections (BRCSs) are evaluated under 2-D periodic boundary conditions for the designed reflectors with a physical size of approximately 70 mm×70 mm consisting of 12 × 136 and 16 × 136 unit cells for the designs with $(\theta_I, \theta_R) = (0°, 45°)$ and $(\theta_I, \theta_R) = (-10°, 50°)$, respectively. Fig. 7 shows the simulated BRCSs of an incident wave with $\theta_I = 0°$ and $-10°$ for the designed reflectors with $(\theta_I, \theta_R) = (0°, 45°)$ and $(\theta_I, \theta_R) = (-10°, 50°)$, respectively. It is noted that each reflection peak corresponds to each diffraction mode excitation and the BRCS patterns in Fig. 7 reflect the diffraction mode power distributions shown in Fig. 6. As seen from Fig. 7, the parasitic reflections are significantly suppressed with the unit cell optimization for both designs and the main reflections are successfully directed into the desired directions of $\theta_R = 45°$ and $50°$ at both two frequencies for the reflectors with $(\theta_I, \theta_R) = (0°, 45°)$ and $(\theta_I, \theta_R) = (-10°, 50°)$, respectively. For the optimized design with $(\theta_I, \theta_R) = (0°, 45°)$, the parasitic reflections are suppressed to -21.1 dB and -13.8 dB from the main peaks at 220 GHz and 293.3 GHz, respectively. For the optimized design with $(\theta_I, \theta_R) = (-10°, 50°)$, the parasitic reflections are suppressed to -14.2 dB and -13.3 dB at 220 GHz and 293.3 GHz, respectively. Note that the designed reflectors exhibit anomalous reflections only for the y-polarized incident wave (see Fig. 1) and reflect the cross-polarized incident wave into the specular direction ($\theta_I = \theta_R$) as a metallic plate.

It is of practical importance to investigate the incident angle dependencies of the anomalous reflection performances as a tolerance test for the incident angle. For the anomalous reflections using the third and fourth diffraction modes, the reflection directions at 220 GHz and 293.3 GHz are equal even when the incident angle θ_i deviates from the design θ_I. However, the reflection angle θ_r deviates from the design θ_R in principle depending on θ_i according to the relation of $\theta_r = \sin^{-1}(\sin\theta_i \pm 4\lambda_0/D_x)$. Considering practical zoning applications toward a specific desired

direction, the anomalous reflection efficiencies for various θ_i are numerically evaluated within a range of $\theta_I - 10° \leq \theta_i \leq \theta_I + 10°$. Fig. 8 shows the simulated incident angle dependencies of the anomalous reflection efficiencies at 220 GHz and 293.3 GHz for the two designs. In the figure, the vertical black dashed line represents the designed θ_I value. As shown in the figure, the anomalous reflection efficiencies at the two frequencies are maintained over a range where θ_i is smaller than the design θ_I. On the other hand, the efficiencies deteriorate rapidly when θ_i becomes larger than the design θ_I. The relation between θ_i and θ_r is represented by a green line in Fig. 8. The decreasing trend of the effciencies would be due to the fact that both θ_r and the steering reflection angle $|\theta_i - \theta_r|$ increases with θ_i.

III. COMPACT REFLECTOR CHARACTERIZATION SYSTEM IN J-BAND EXPLOITING CATR TECHNIQUE

In this section, we introduce a compact reflector characterization system in the J-band exploiting the CATR technique. In the developed system, a quasi-plane wave generated by reflecting mirrors illuminates a reflector sample and scattered wave distributions are obtained to measure far-field BRCS of the sample. The system configuration and its performance evaluation in terms of the planarity of the generated quasi-plane wave are presented in Section III-A and III-B, respectively.

A. SYSTEM CONFIGURATION

Fig. 9 shows the J-band reflector characterization system exploiting the CATR technique developed to evaluate the reflection characteristics of anomalous reflectors under plane wave illumination. The system is based on an offset Gregorian antenna consisting of parabolic and ellipsoidal mirrors to generate a quasi-plane wave in a short range with a wide beamwidth. The diameter of the main parabolic mirror is 1210 mm, and the major and minor diameters of the secondary ellipsoidal mirror are 300 mm and 206 mm, respectively. The widths of the parabolic and ellipsoidal mirror apertures are 535 mm and 315 mm, respectively. The surface roughness of the mirror surfaces is less than 5 µm. A J-band conical corrugated-horn antenna with a gain of 18 dBi positioned at the focal point of the ellipsoidal mirror is used for the feed antenna. A reflector sample is located at a position approximately 900 mm from the parabolic surface center. The sample is illuminated from the offset Gregorian antenna with an incident azimuth angle of θ_I. By rotating a probe antenna around the sample with an automated rotation table, the angle dependencies of the reflection characteristics are measured in the scanning range of $-90° \leq \theta \leq 90°$ with the interval of $\Delta\theta = 0.5°$. A J-band conical horn antenna with a gain of 20 dBi is used for the probe antenna, and the distance between the probe antenna and the sample is set to be $R = 400$ mm. The feed and probe antennas are aligned so that the polarization is oriented vertically. The transmittance S_{21} between the feed and probe antennas is measured in the frequency range from 220 GHz to 330 GHz

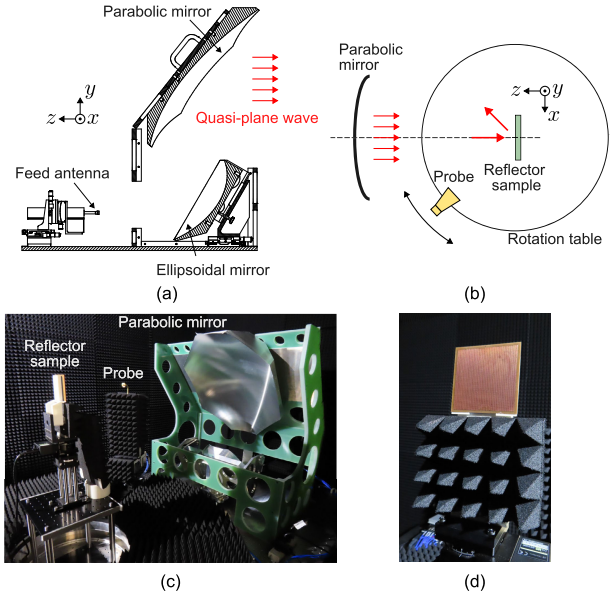

FIGURE 9. Developed reflector characterization system. (a) Schematic of an offset Gregorian antenna to generate a quasi-plane wave. (b) Experimental setup for reflector measurements. Photographs of (c) the reflector characterization system and (d) a reflector sample.

by a Keysight vector network analyzer P5024A with VDI frequency multipliers N5262BW03. In the measurements, the time domain gating is performed on the measured data in order to remove the effect of multiple reflections.

From the near-field S_{21} data acquired by the probe antenna, the far-field BRCSs σ are calculated with the near-field to far-field transformation using the following [26]:

$$\sigma(\theta_r) = A \left| \sum_{m=-\infty}^{+\infty} \frac{j^m e^{jm\theta_r}}{H_m^{(2)}(k_0 R)} \int_{-90°}^{90°} S_{21}(R, \theta) e^{-jm\theta} d\theta \right|^2, \tag{1}$$

where θ_r is the reflection angle, $H_m^{(2)}$ is the Hankel function of the second kind of order m, k_0 is the wavenumber in free space, and A is a constant. Here, A is determined by measuring the BRCSs of a metallic plate with a size of 70 mm×70 mm.

B. PLANARITY OF GENERATED QUASI-PLANE WAVE

To evaluate the planarity of the generated quasi-plane wave, the 2-D electric-field distribution of the generated wave is measured at 300 GHz on the plane including the reflector sample center. The measurement ranges are 0 mm $\leq x \leq$ 680 mm and 0 mm $\leq y \leq$ 640 mm with the interval of $\Delta x = \Delta y = 0.4$ mm (= 0.4 wavelength at 300 GHz). Fig. 10(a) and (b) shows the measured amplitude and phase distributions, respectively. As seen in the figures, an octahedral region having almost flat amplitude and phase distributions is confirmed.

To quantitatively investigate the planarity of the generated wave, the generated wave is decomposed as a sum of plane waves by calculating the Fourier spectrum of the measured electric-field distribution. The result is shown in Fig. 10(c). It is seen from Fig. 10(c) that there exists a sharp peak

at $k_x = k_y = 0$ corresponding to the normal incident plane wave component to the measurement plane, where k_x and k_y are the wavenumber components in the x- and y-directions, respectively. According to the figure, the energy is concentrated in the vicinity of $k_x = k_y = 0$; for instance, 98.6 % of the total radiation power is in the region of $\sqrt{k_x^2 + k_y^2} \leq 0.05k_0$. Other plane wave components originate from various contributions, including scattering from mirror edges, surface roughness of the mirrors, and misalignment between the mirrors and the feed antenna. However, they are significantly suppressed to be less than −50 dB compared to the main peak. Fig. 10(d) shows the Fourier spectrum along $k_x = 0$ and $k_y = 0$ extracted from Fig. 10(c). From the measured main peak width at $k_x = k_y = 0$, the beam size of the generated wave is estimated to be 252 mm in diameter.

The standard deviations of the amplitude and phase distributions in the center region with a diameter of 252 mm are calculated from Fig. 10(a) and (b) to be 1.5 dB and 25.7°, respectively. It is noted that, to illuminate a reflector sample with a beam having such flat amplitude and phase distributions over the large region, a considerable distance from a transmitting antenna is generally required. For instance, when the corrugated horn antenna used as the feed antenna in the developed system is used as a transmitting antenna, the distance needs to be longer than 30 m, according to additional simulations on the basis of the method of moments using FEKO. In contrast, the distance between the parabolic mirror and the reflector sample is as short as 900 mm in the developed CATR-based reflector characterization system. The compact system size contributes to reduce cable and free-space propagation losses in the J-band, enabling highly accurate measurements with a large signal-to-noise ratio.

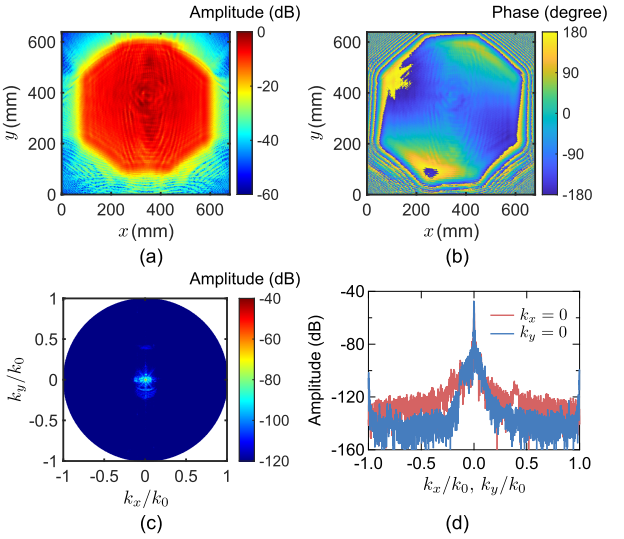

FIGURE 10. Measured electric-field distribution of the generated quasi-plane wave. Measured (a) amplitude and (b) phase distributions on the scanning plane 900 mm away from the parabolic mirror center. (c) Fourier spectrum of the measured electric-field distribution. (d) Fourier spectrum along $k_x = 0$ and $k_y = 0$ extracted from (c).

IV. DUAL-BAND REFLECTOR PERFORMANCES

A. PROTOTYPES

To experimentally demonstrate the dual-band anomalous reflection characteristics in the J-band, the designed reflectors for $(\theta_I, \theta_R) = (0°, 45°)$ and $(-10°, 50°)$ are fabricated on the 0.05 mm-thick COP substrates with 12 µm-thick copper metallic patterns using lithography and electroplating techniques. The metallic pattern area of each prototype is 70 mm×70 mm consisting of 12 × 136 and 16 × 136 unit cells. The total sample size is 75 mm×75 mm. Based on the laser microscope observations, we confirm that the deviations of the metallic patch dimensions from the design values are less than 4 µm and the rounded patch corner radii are less than 5 µm. Each prototype is adhered to a phenolic resin plate to hold thin and flexible prototypes straight and flat. In the measurements, each prototype is fixed in the center of the quasi-plane wave region with almost flat amplitude and phase distributions in Fig. 10(a) and (b).

B. RESULTS AND DISCUSSION

Fig. 11(a) and (b) shows the measured BRCSs of the reflectors for $(\theta_I, \theta_R) = (0°, 45°)$ and $(-10°, 50°)$, respectively, plotted against the reflection angle θ_r and frequency f. The dashed lines in the figures represent the theoretical relationship between θ_r and f obtained using the following equation for the m-th diffraction mode:

$$\sin\theta_r = \sin\theta_I + \frac{mc_0}{fD_x}, \tag{2}$$

where c_0 is the speed of light. As seen in the figures, specular ($m = 0$) and anomalous ($m \neq 0$) reflections with various diffraction modes are clearly observed as loci of maxima, and their positions are in excellent agreement with the theoretical prediction of the dashed lines. Strong anomalous reflections near 220 GHz and 293.3 GHz in the designed θ_R direction are confirmed for both prototypes with suppressed parasitic reflections in other directions. Fig. 11(c) and (d) shows the simulated BRCSs of the reflectors for $(\theta_I, \theta_R) = (0°, 45°)$ and $(-10°, 50°)$, respectively, calculated under 2-D periodic boundary conditions for the reflectors with the same size as the prototypes. The measured BRCSs are quantitatively in good agreement with the simulated results, suggesting the accurate design, fabrication, and characterization of the reflectors.

The frequency dependencies of the diffraction modes can be extracted from the measured BRCSs along the dashed lines. Fig. 12(a) and (b) shows the extracted results for $(\theta_I, \theta_R) = (0°, 45°)$ and $(-10°, 50°)$ obtained from Fig. 11(a) and (b), respectively. As seen from the figures, for both two reflectors, the diffraction modes with $m = 3$ and 4 corresponding to the desired anomalous reflections have peaks near 220 GHz and 293.3 GHz, respectively, with significantly suppressed parasitic reflections including the specular reflection with $m = 0$ at the two frequencies. For the reflector with $(\theta_I, \theta_R) = (0°, 45°)$

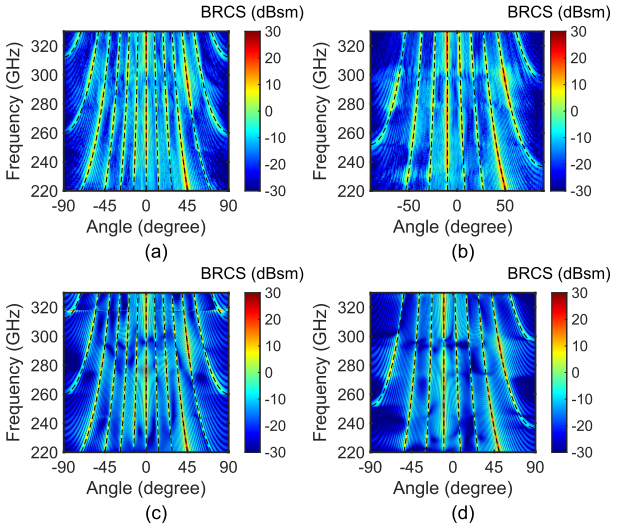

FIGURE 11. Measured BRCSs of the reflectors for (a) $(\theta_I, \theta_R) = (0°, 45°)$ and (b) $(\theta_I, \theta_R) = (-10°, 50°)$. Simulated BRCSs of the reflectors for (c) $(\theta_I, \theta_R) = (0°, 45°)$ and (d) $(\theta_I, \theta_R) = (-10°, 50°)$. Dashed lines: theoretical relationship between the reflection angle and frequency for diffraction modes observed in the measurements.

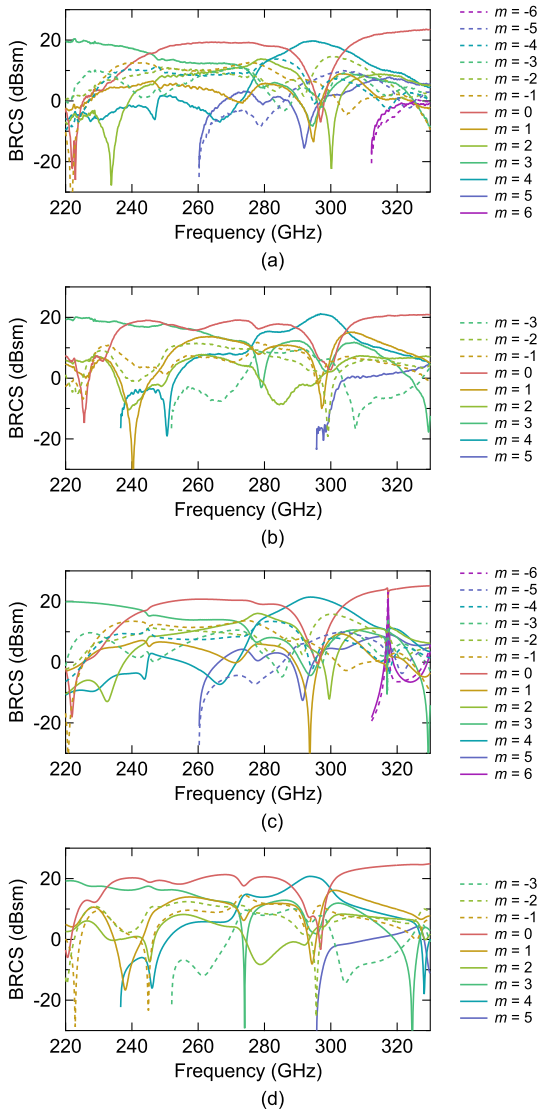

FIGURE 12. Measured frequency dependencies of the BRCSs for the diffraction modes for (a) $(\theta_I, \theta_R) = (0°, 45°)$ and (b) $(\theta_I, \theta_R) = (-10°, 50°)$ extracted from Fig. 11(a) and (b), respectively. Simulated reflection characteristics of the diffraction modes for (c) $(\theta_I, \theta_R) = (0°, 45°)$ and (d) $(\theta_I, \theta_R) = (-10°, 50°)$ extracted from Fig. 11(c) and (d), respectively.

(Fig. 12(a)), the parasitic reflections are suppressed to −19.1 dB and −11.4 dB compared to the anomalous reflections at 220 GHz and 293.3 GHz, respectively. For the reflector with $(\theta_I, \theta_R) = (-10°, 50°)$ (Fig. 12(b)), the parasitic reflections are suppressed to −11.7 dB and −6.3 dB compared to the anomalous reflections at 220 GHz and 293.3 GHz, respectively. Fig. 12(c) and (d) shows the corresponding simulated reflection characteristics of the diffraction modes for $(\theta_I, \theta_R) = (0°, 45°)$ and $(-10°, 50°)$, respectively, extracted from Fig. 11(c) and (d) along the dashed lines. Comparing the measured and simulated results in Fig. 12, they are in good overall agreement, except that the measured reflection characteristics for the reflector with $(\theta_I, \theta_R) = (-10°, 50°)$ are slightly shifted to higher frequencies compared to the simulated results. Incidentally, the resonant behavior at 317 GHz for the reflector with $(\theta_I, \theta_R) = (0°, 45°)$ confirmed in the simulated results in Fig. 12(c) is not observed in the measured results in Fig. 12(a). The cause of this is not identified yet but might be due to a numerical singularity in the simulations under infinite periodic boundary conditions.

To investigate the behavior near the operating frequencies, the total parasitic reflections are calculated from Fig. 12 near 220 GHz and 293.3 GHz by summing the reflected powers of all diffraction modes except for the desired anomalous reflections with $m = 3$ and 4, respectively. Fig. 13 shows the obtained total parasitic reflections (blue lines), as well as the desired anomalous reflections (red lines), in the frequency ranges from 220 GHz to 230 GHz and from 290 GHz to 305 GHz. In the figures, the solid and dashed lines represent the measured and simulated results, respectively. Fig. 13(a) and (b) shows the results for $(\theta_I, \theta_R) = (0°, 45°)$ and $(-10°, 50°)$, respectively. For the reflector with $(\theta_I, \theta_R) = (0°, 45°)$, the measured frequency characteristics agree well with the simulated results, except for a slight downward BRCS shift in the higher band. The measured total parasitic reflection levels compared to the desired anomalous reflections have local minima of −14.2 dB and −5.8 dB at 220.7 GHz and 294.3 GHz, respectively. For the reflector with $(\theta_I, \theta_R) = (-10°, 50°)$, the measured results are slightly shifted to higher frequencies compared with the simulated results. The measured total parasitic reflection levels compared to the desired anomalous reflections have local minima of −12.0 dB and −10.0 dB at 225.2 GHz and 297.6 GHz, respectively. The frequency shifts from the designed values of 220 GHz and 293.3 GHz are considered to be due to prototyping errors in fabrications.

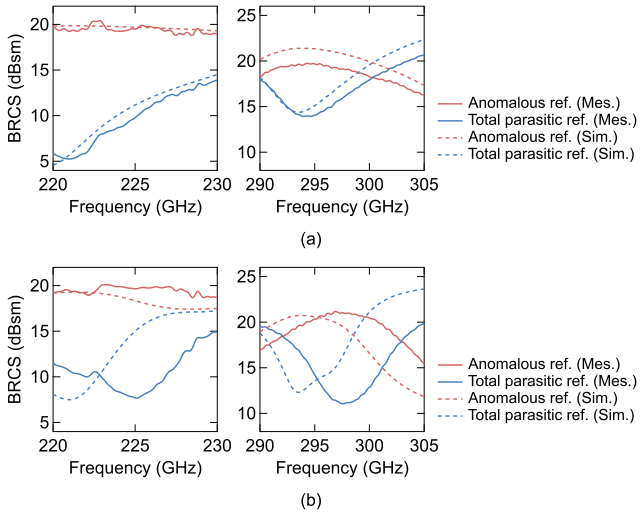

FIGURE 13. Frequency dependences of the anomalous reflections and the total parasitic reflections near the designed frequencies for (a) $(\theta_I, \theta_R) = (0°, 45°)$ and (b) $(\theta_I, \theta_R) = (-10°, 50°)$, respectively. Solid and dashed lines represent the measured and simulated results, respectively.

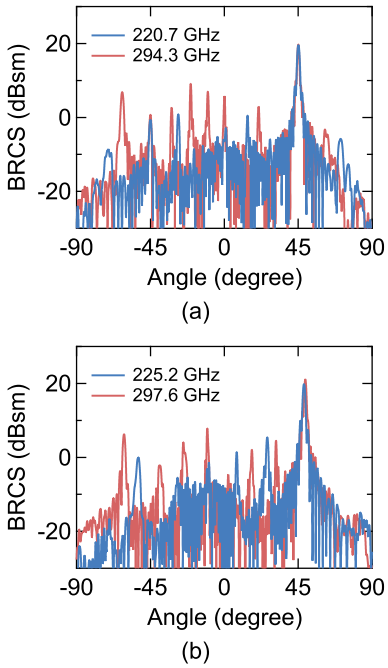

FIGURE 14. Measured angle dependencies of the BRCSs at the two frequencies where the total parasitic reflections are minimized. (a) Results for the prototype with $(\theta_I, \theta_R) = (0°, 45°)$ at 220.7 GHz and 294.3 GHz. (b) Results for the prototype with $(\theta_I, \theta_R) = (-10°, 50°)$ at 225.2 GHz and 297.6 GHz.

Note that the prototype for $(\theta_I, \theta_R) = (-10°, 50°)$ has narrower and more densely formed metallic patches and would be more susceptible to prototyping errors (see Fig. 4 and 5).

Fig. 14 shows the measured angle dependencies of the BRCSs for $(\theta_I, \theta_R) = (0°, 45°)$ and $(-10°, 50°)$ at the two frequencies where the total parasitic reflections are minimized (at 220.7 GHz and 294.3 GHz for the prototype with $(\theta_I, \theta_R) = (0°, 45°)$, and at 225.2 GHz and 297.6 GHz for the prototype with $(\theta_I, \theta_R) = (-10°, 50°)$). As seen from Fig. 14, the main reflections are directed into the desired θ_R direction with significantly suppressed parasitic reflections at both two frequencies for both designs, as predicted in the simulation results of Fig. 7. The differences between the measured BRCS peak angles at these frequencies and the designed θ_R values are less than 0.1° and 1.5° for $(\theta_I, \theta_R) = (0°, 45°)$ and $(-10°, 50°)$, respectively. For the prototype with $(\theta_I, \theta_R) = (0°, 45°)$, the parasitic reflections are suppressed to −18.7 dB and −10.6 dB from the main peaks at 220.7 GHz and 294.3 GHz, respectively. For the prototype with $(\theta_I, \theta_R) = (-10°, 50°)$, the parasitic reflections are suppressed to −14.4 dB and −13.3 dB at 225.2 GHz and 297.6 GHz, respectively.

The reflection efficiency $\left|S_{11}^{0\to m}\right|^2$ is calculated from each of the measured BRCS peaks corresponding to each diffraction mode by compensating for the sample size and incident/reflection angles with the following factor η [1]:

$$\eta = \frac{4\pi f^2 S^2}{c_0^2} \cos\theta_I \cos\theta_r, \tag{3}$$

where S is the metallic pattern area of the reflector. Then, as in Section II-B, the anomalous reflection efficiency, the energy leakage to the parasitic reflections, the material losses in the substrate, and the efficiency excluding the material losses are obtained by calculating $\left|S_{11}^{0\to m^*}\right|^2$, $\sum_{m\neq m^*}\left|S_{11}^{0\to m}\right|^2$, $\left(1-\sum_m\left|S_{11}^{0\to m}\right|^2\right)$, and $\left|S_{11}^{0\to m^*}\right|^2 / \sum_m\left|S_{11}^{0\to m}\right|^2$, respectively. Table 3 and 4 summarize the results for the prototypes with $(\theta_I, \theta_R) = (0°, 45°)$ and $(-10°, 50°)$, respectively.

As seen from Table 3 and 4, highly efficient dual-band anomalous reflection operation is experimentally demonstrated for both designs with the efficiency excluding the material losses of as high as 96.4 %/80.5 % for the lower and higher bands of the prototype with $(\theta_I, \theta_R) = (0°, 45°)$ and 95.3 %/91.6 % for the lower and higher bands of the prototype with $(\theta_I, \theta_R) = (-10°, 50°)$. From the comparison with the simulated results in Table 1 and 2, each measured value agrees well with the corresponding simulated value of the optimized designs. The largest discrepancies between the measured and simulated results are seen for the efficiency and material loss for $(\theta_I, \theta_R) = (0°, 45°)$ at the higher band. In general, the discrepancies can be attributed to various contributions in the J-band, including those originated from the sample such as prototyping errors in fabrications, scattering from the sample edges due to the finite sample size, and inaccuracy of material parameters used in the design, as well as those from the measurements such as sample and antenna misalignments, uncertainties in transmission measurements using the vector network analyzer, and residual non-uniformity of the incident wave at the sample plane. Note that the measured efficiency excluding the material loss is still higher than 80 % for both lower and higher bands of both designs, which is consistent

TABLE 3. Measurement results of the efficiencies, loss contributions owing to parasitic reflections and material losses, and efficiencies excluding the material losses for the prototype with $(\theta_I, \theta_R) = (0°, 45°)$.

Frequency	Efficiency	Total parasitic reflection	Material loss	Efficiency excl. material loss
220.7 GHz	80.6 %	3.0 %	16.4 %	96.4 %
294.3 GHz	47.8 %	11.6 %	40.6 %	80.5 %

TABLE 4. Measurement results of the efficiencies, loss contributions owing to parasitic reflections and material losses, and efficiencies excluding the material losses for the prototype with $(\theta_I, \theta_R) = (-10°, 50°)$.

Frequency	Efficiency	Total parasitic reflection	Material loss	Efficiency excl. material loss
225.2 GHz	87.6 %	4.3 %	8.1 %	95.3 %
297.6 GHz	69.5 %	6.4 %	24.1 %	91.6 %

with the simulation predictions in Table 1 and 2 and would be acceptable for practical applications.

V. CONCLUSION

We have proposed the dual-band reflectors operating at 220 GHz and 293.3 GHz achieving highly efficient dual-band anomalous reflections in identical directions with wide steering reflection angles for 6G applications. The dual-band anomalous reflections are realized by controlling higher-order diffraction modes simultaneously at the two frequencies with paired patch elements. The proposed reflector design on a single-layer and via-free substrate has the advantage of being simple configuration and practical in terms of implementation in the sub-terahertz and terahertz bands. In addition, we have developed the compact reflector characterization system in the J-band exploiting the CATR technique, in which the generated quasi-plane wave with a beam diameter of approximately 250 mm at 300 GHz is used to perform accurate far-field BRCS measurements of large reflectors under plane wave illumination. We have designed and fabricated the dual-band reflectors on the COP substrates for $(\theta_I, \theta_R) = (0°, 45°)$ and $(-10°, 50°)$ and evaluated their dual-band anomalous reflection performances using the developed CATR-based reflector characterization system. We have confirmed that the measured BRCSs of the prototypes are in good agreement with the simulated results, suggesting the accurate design, fabrication, and characterization of the reflectors. We have experimentally demonstrated highly efficient dual-band anomalous reflection operations of the designed reflectors at 220 GHz and 293.3 GHz with the efficiencies excluding the material losses of over 80 % with suppressed parasitic reflections in undesired directions. Although the proposed dual-band anomalous reflectors have limitations in that they can only operate in a single polarization and their operating frequencies must be related to each other by a simple integer ratio, the reflectors are promising to be used for coverage expansion in carrier aggregated 6G wireless communication owing to their highly efficient operation with simple configuration. Future research includes realizing dual-band anomalous reflectors operating with both polarizations, demonstrating communication coverage expansion using the developed reflectors, and evaluating the developed reflector characterization system performance in other frequency bands.

REFERENCES

[1] A. Díaz-Rubio, V. S. Asadchy, A. Elsakka, and S. A. Tretyakov, "From the generalized reflection law to the realization of perfect anomalous reflectors," *Sci. Adv.*, vol. 3, no. 8, Aug. 2017, Art. no. e1602714.
[2] Y. Ra'di, D. L. Sounas, and A. Alù, "Metagratings: Beyond the limits of graded metasurfaces for wave front control," *Phys. Rev. Lett.*, vol. 119, no. 6, Aug. 2017, Art. no. 067404.
[3] A. M. H. Wong and G. V. Eleftheriades, "Perfect anomalous reflection with a bipartite Huygens' metasurface," *Phys. Rev. X*, vol. 8, no. 1, Feb. 2018, Art. no. 011036.
[4] C. Liaskos, S. Nie, A. Tsioliaridou, A. Pitsillides, S. Ioannidis, and I. Akyildiz, "A new wireless communication paradigm through software-controlled metasurfaces," *IEEE Commun. Mag.*, vol. 56, no. 9, pp. 162–169, Sep. 2018.
[5] O. Rabinovich, I. Kaplon, J. Reis, and A. Epstein, "Experimental demonstration and in-depth investigation of analytically designed anomalous reflection metagratings," *Phys. Rev. B, Condens. Matter*, vol. 99, no. 12, Mar. 2019, Art. no. 125101.
[6] E. Basar, M. Di Renzo, J. De Rosny, M. Debbah, M.-S. Alouini, and R. Zhang, "Wireless communications through reconfigurable intelligent surfaces," *IEEE Access*, vol. 7, pp. 116753–116773, 2019.
[7] Q. Wu and R. Zhang, "Towards smart and reconfigurable environment: Intelligent reflecting surface aided wireless network," *IEEE Commun. Mag.*, vol. 58, no. 1, pp. 106–112, Jan. 2020.
[8] Y. Kato, K. Omori, and A. Sanada, "D-band perfect anomalous reflectors for 6G applications," *IEEE Access*, vol. 9, pp. 157512–157521, 2021.
[9] J.-B. Gros, V. Popov, M. A. Odit, V. Lenets, and G. Lerosey, "A reconfigurable intelligent surface at mmWave based on a binary phase tunable metasurface," *IEEE Open J. Commun. Soc.*, vol. 2, pp. 1055–1064, 2021.
[10] Y. Kato, K. Yonemura, K. Seki, R. Kambara, and A. Sanada, "Reconfigurable anomalous reflectors with stretchable elastic substrates at 140 GHz band," *Nanophotonics*, vol. 12, no. 13, pp. 2527–2535, Jun. 2023.
[11] H. Hashiguchi, T. Nishime, N. Michishita, H. Morishita, H. Matsuno, T. Ohto, and M. Nakano, "Dual bands and dual polarization reflectarray for millimeter wave application by supercell structure," *IEICE Trans. Commun.*, vol. E106.B, no. 3, pp. 241–249, 2023.
[12] G. Xu, S. V. Hum, and G. V. Eleftheriades, "Dual-band reflective metagratings with interleaved meta-wires," *IEEE Trans. Antennas Propag.*, vol. 69, no. 4, pp. 2181–2193, Apr. 2021.
[13] R. S. Malfajani and Z. Atlasbaf, "Design and implementation of a dual-band single layer reflectarray in X and K bands," *IEEE Trans. Antennas Propag.*, vol. 62, no. 8, pp. 4425–4431, Aug. 2014.
[14] S.-W. Qu, Q.-Y. Chen, M.-Y. Xia, and X. Y. Zhang, "Single-layer dual-band reflectarray with single linear polarization," *IEEE Trans. Antennas Propag.*, vol. 62, no. 1, pp. 199–205, Jan. 2014.
[15] Z. Hamzavi-Zarghani and Z. Atlasbaf, "A new broadband single-layer dual-band reflectarray antenna in X- and Ku-bands," *IEEE Antennas Wireless Propag. Lett.*, vol. 14, pp. 602–605, 2015.

[16] R. Deng, S. Xu, F. Yang, and M. Li, "Single-layer dual-band reflectarray antennas with wide frequency ratios and high aperture efficiencies using Phoenix elements," *IEEE Trans. Antennas Propag.*, vol. 65, no. 2, pp. 612–622, Feb. 2017.
[17] X. Li, X. Li, and L. Yang, "Single-layer dual-band wide band-ratio reflectarray with orthogonal linear polarization," *IEEE Access*, vol. 8, pp. 93586–93593, 2020.
[18] S. Costanzo, F. Venneri, A. Borgia, and G. D. Massa, "Dual-band dual-linear polarization reflectarray for mmWaves/5G applications," *IEEE Access*, vol. 8, pp. 78183–78192, 2020.
[19] Z. P. Li, J. Ala-Laurinaho, Z. Du, and A. V. Räisänen, "Realization of wideband hologram compact antenna test range by linearly adjusting the feed location," *IEEE Trans. Antennas Propag.*, vol. 62, no. 11, pp. 5628–5633, Nov. 2014.
[20] C. Liu and X. Wang, "Design and test of a 0.3 THz compact antenna test range," *Prog. Electromagn. Res. Lett.*, vol. 70, pp. 81–87, 2017.
[21] J. Yu, H. Yu, T. Chen, J. Wang, Y. Yao, and X. Chen, "Application of compact antenna test range in terahertz antenna measurement," in *Proc. Cross Strait Radio Sci. Wireless Technol. Conf. (CSRSWTC)*, Dec. 2020, pp. 1–3.
[22] Z. Li, P. Huo, Y. Wu, and J. Wu, "Reflectarray compact antenna test range with controlled aperture disturbance fields," *IEEE Antennas Wireless Propag. Lett.*, vol. 20, no. 7, pp. 1283–1287, Jul. 2021.
[23] J. Su, H. He, Z. Li, Y. Yang, H. Yin, and J. Wang, "Uneven-layered coding metamaterial tile for ultra-wideband RCS reduction and diffuse scattering," *Sci. Rep.*, vol. 8, no. 1, p. 8182, May 2018.
[24] P. Yang, Y. Xiao, M. Xiao, and S. Li, "6G wireless communications: Vision and potential techniques," *IEEE Netw.*, vol. 33, no. 4, pp. 70–75, Jul. 2019.
[25] T. Kürner and A. Hirata, "On the impact of the results of WRC 2019 on THz communications," in *Proc. 3rd Int. Workshop Mobile THz Syst. (IWMTS)*, Jul. 2020, pp. 1–3.
[26] C. Parini, S. Gregson, J. McCormick, and D. J. van Rensburg, *Theory and Practice of Modern Antenna Range Measurements*. London, U.K.: IET, 2014.

YUTO KATO (Member, IEEE) received the B.S. and M.S. degrees in physics from The University of Tokyo, Tokyo, Japan, in 2010 and 2012, respectively, and the Ph.D. degree from Osaka University, Osaka, Japan, in 2020.

Since 2012, he has been with the National Metrology Institute of Japan, National Institute of Advanced Industrial Science and Technology, Tsukuba, Japan. His current research interests include material characterizations and electromagnetic metasurfaces at microwave and millimeter-wave frequencies.

Dr. Kato is an Associate Editor of IEEE TRANSACTIONS ON INSTRUMENTATION AND MEASUREMENT.

MICHITAKA AMEYA (Member, IEEE) received the B.E. and M.E. degrees from the Department of Electronic Engineering, Hokkaido University, Hokkaido, Japan, in 2003 and 2005, respectively, and the Ph.D. degree from the Graduate School of Information Science and Technology, Hokkaido University, in 2008.

He has been a Senior Researcher with the National Metrology Institute of Japan, National Institute of Advanced Industrial Science and Technology, Tsukuba, Japan, since 2008. His current research interests include electromagnetic compatibility, millimeter-wave antenna calibration, terahertz antenna measurement, RCS measurement, and 5G & 6G array antenna testing by machine learning algorithm.

MASAO TEZUKA received the B.E. and M.E. degrees in applied physics from Hokkaido University, Hokkaido, Japan, in 1988 and 1990, respectively. Since 1990, he has been with TDK Corporation.

HISASHI KOBUKE received the B.S. degree in physics from Rikkyo University, Tokyo, Japan, in 1986. Since 1986, he has been with TDK Corporation.

ATSUSHI SANADA (Member, IEEE) received the B.E., M.E., and Ph.D. degrees in electronics engineering from Okayama University, Okayama, Japan, in 1989, 1991, and 1994, respectively.

From 1994 to 1995 and from 2002 to 2003, he was a Visiting Scholar with the University of California at Los Angeles, Los Angeles, CA, USA. He was a Visiting Scholar with the Advanced Telecommunications Research Institute International, Seika, Japan, from 2004 to 2005, and Japan Broadcasting Corporation, Tokyo, Japan, in 2005. In 2016, he joined the Graduate School of Engineering Science, Osaka University, Osaka, Japan, where he is currently a Professor. His current research interests include microwave science and technologies, including metamaterials, transformation electromagnetics, high-Tc superconducting devices, and ferrite devices.

Dr. Sanada is a member of the European Microwave Association and the Institute of Electronics, Information and Communication Engineers (IEICE), Japan, and the European Microwave Association (EuMA). He has served as an elected member for the Administrative Committee of the IEEE Microwave Theory and Techniques Society (MTT-S), from 2015 to 2020, the MTT-S Region 10 Coordinator, from 2011 to 2020, and has been the Chapter Chair for the MTT-S Kansai Chapter, since 2019.